



Analysis of the thermal expansion and mechanical properties of laser cladding of Invar alloy

Shichao Zhu¹ · Baolin Niu² · Zhen Chang³ · Bing Long¹ · Feihong Yin¹ · Linhan Ouyang⁴ · Lingling Xie⁵ · Zhengyi Jiang⁶

Received: 31 July 2023 / Accepted: 3 March 2024 / Published online: 9 March 2024
© The Author(s), under exclusive licence to Springer-Verlag London Ltd., part of Springer Nature 2024

Abstract

Laser cladding has significant advantages in the forming process of Invar alloy. Nevertheless, the coefficient of thermal expansion, microstructure and mechanical properties still need to be further investigated. In this paper, the Invar alloy powder was used to prepare cladding samples, and the performance and microstructure of the cladding layer were investigated. The mechanical and thermal expansion performances of the cladding layer were analysed using a universal material testing machine and a thermal expansion instrument, and the microscopic structure and micro zone composition of the tensile fracture of the cladding layer were investigated using an SEM scanning electron microscope and an EDS energy spectrum analyser. The results show that the mechanical properties of the Invar alloy transverse cladding layer are better than those of longitudinal cladding layer; the thermal expansion performance of the cladding layer is good, and it keeps the same with the base material in the range of 25–200 °C; the fracture analysis reveals more dimples in the transverse cladding layer fracture with better plastic tenacity, and intergranular fracture and quasi-cleavage fracture in the longitudinal cladding layer fracture with slightly poor plastic tenacity.

Keywords Laser cladding · Thermal expansion · Mechanical properties · Multi-pass and multi-layer

✉ Shichao Zhu
zhushichao888@126.com

✉ Lingling Xie
xll@ahut.edu.cn

✉ Zhengyi Jiang
jiang@uow.edu.au

¹ College of Aeronautics and Mechanical Engineering, Changzhou Institute of Technology, Changzhou 213002, People's Republic of China

² China Aviation Development Aviation Technology Co., Ltd, Chengdu 610503, People's Republic of China

³ Hangzhou Bearing Test & Research Center, Hangzhou 310022, People's Republic of China

⁴ College of Economics and Management, Nanjing University of Aeronautics and Astronautics, Nanjing 211106, People's Republic of China

⁵ College of Metallurgical Engineering, Anhui University of Technology, Maanshan 243032, People's Republic of China

⁶ School of Mechanical, Materials, Mechatronic and Biomedical Engineering, University of Wollongong, Wollongong, NSW 2522, Australia

1 Introduction

As a new type of surface modification technology, laser cladding improves the surface properties of materials by melting metal powder onto the surface of the substrate to manufacture a variety of alloy coatings with excellent properties [1, 2]. At present, laser cladding technology has broad development prospects in aerospace, navigation, medical, military and other fields [3, 4]. Laser cladding technology can not only repair the surface failure of components, but also produce coatings that can improve the mechanical and chemical properties of the workpiece, increasing its adaptability to harsh working environments and service life [5–7]. Because of their special thermal expansion performance, Invar alloys are widely used. However, defects in mechanical and physicochemical properties limit their scope of use. Laser cladding technology plays a prominent role in enhancing and reinforcing Invar alloy as well as broadening its applications [8].

The mechanical performance index of the cladding layer can reflect the quality of the cladding layer macroscopically. Currently, the research on laser cladding focuses on the control of process parameters, while few studies on the properties of

Invar alloy cladding layer have been reported. As a result, by studying the mechanical properties of the cladding layer, many significant mechanical performance indexes can be obtained, allowing the cladding layer's quality to be evaluated to some extent. Li et al. [9] adopted the rectangular tensile test method on the multi-pass and multi-layer laser cladding layer of 45 and 9Cr2Mo steels, which considerably enhanced experimental efficiency and completed the test for cladding layer mechanical properties. Wu [10] studied the mechanical properties of titanium alloy prepared by SLM technology through tensile test. The research shows that the density, elastic modulus and yield strength of Ti64 lattice structure are closely related to the aspect ratio and angle of the rod. Sun et al. [11] studied the mechanical properties of aluminium alloy induced by laser shock peening through tensile test. The experimental results show that the tensile strength, yield strength and elongation of the aluminum alloy strengthened by laser shot peening are improved by comparing with the matrix.

The cladding layer often has defects such as cracks and pores, which have significant impact on the thermal expansion coefficient. To avoid such defects, it is vital to select the cladding material with properties equivalent to the base metal when selecting and proportioning the cladding powder. In the meantime, for some metals with special thermal expansion performance, the thermal expansion performance of the cladding layer needs to be closer to the base metal, so it is more essential to research these properties. Harrison et al. [12] studied the thermal expansion behaviour of Invar alloy treated by SLM process, and they found that the thermal expansion coefficient of SLM processed Invar alloy is lower than that of traditional methods, which is ascribed to the effects of residual stress. Qiu et al. [13] studied the microstructure and properties of Invar alloy treated by SLM process, and it is found that the thermal expansion performance of Invar alloy treated by SLM process and traditional process is equivalent below 300 °C. Asgari et al. [14] studied the microstructure and properties of Invar alloy cladding with different laser powers, and experiments showed that the thermal expansion coefficient of the sample made under the optimized laser power is extremely low, and it is comparable to that of the Invar alloy made by the traditional method.

Although there have been ample researches, the reports on the mechanical properties and thermal expansion performance of the Invar alloy laser cladding layer are relatively rare. Therefore, the mechanical performance, thermal expansion performance, and fracture microstructure of the Invar alloy laser cladding layer were investigated in this paper. Scanning electron microscopy (SEM) was used to observe the fracture

morphology of the tensile samples in order to analyse the fracture properties, and X-ray energy-dispersive spectrometer (EDS) was employed to analyse the fracture composition [15–18]. By comparing the fracture characteristic of the cladding layer and the substrate sample, it is possible to determine whether the properties of the cladding layer meet the requirements of the base metal [19–21]. Additionally, it helps to further improve the process parameters [22, 23] to obtain the best laser cladding process parameters.

2 Experimental

2.1 Material

The Invar alloy substrate in this experiment was produced by the French Pulang Alloy Co., Ltd. (Paris, France) and was supplied by Shanghai Aircraft Manufacturing Co., Ltd. (Shanghai, China). Next, upon the experimental requirements, the substrate was processed with the dimension of 100 mm × 50 mm × 20 mm. Besides, the powder particles were fabricated through the plasma rotating electrode. The chemical compositions of substrate and particles are illustrated in Table 1. The thermophysical properties of the Invar alloy were presented by Leica scanning electron microscope (Bruker, Germany) shown in Table 2. The elemental composition of the particles was detected via SciAps energy-dispersive X-ray spectroscopy (Boston, American), as presented in Fig. 1a. The morphological (size and shape) of the powder was detected with SEM, and the radius of the particles was performed to be in the size range of 60–140 μm using a Leica scanning electron microscope (Bruker, Germany), as presented in Fig. 1b.

2.2 Experimental equipment and methods

As shown in Fig. 2, the laser cladding equipment employs a 6 kW continuous Nd:YAG laser system (Trumpf, Germany), a gas protection system, a powder particle feeding system, and a control system. The technological parameters of the

Table 2 Behaviours of Invar alloy

Elongation $\delta(\%)$	Density $g(\text{cm}^{-3})$	Hardness HV	Tensile strength $\sigma_b(\text{MPa})$	Modulus of elasticity (MPa)	Thermal conductivity $W \cdot (\text{mK})^{-1}$
30	8.12	140	500	134,000	0.109~0.134

Table 1 Elemental composition of Invar alloy

S	C	Mn	Fe	Ni	Cr	Co	Si	P
0.001	0.025	0.27	63.0	35.92	0.20	0.47	0.07	0.0087

Fig. 1 Elemental composition and morphology of Invar alloy particles. **a** Elemental composition and **b** morphology

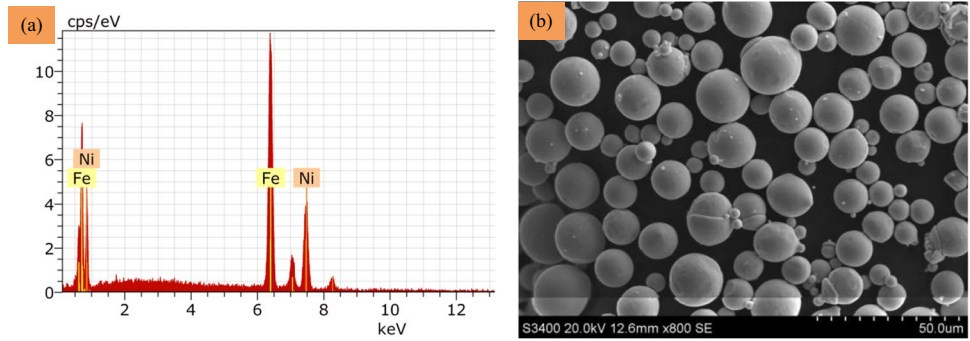
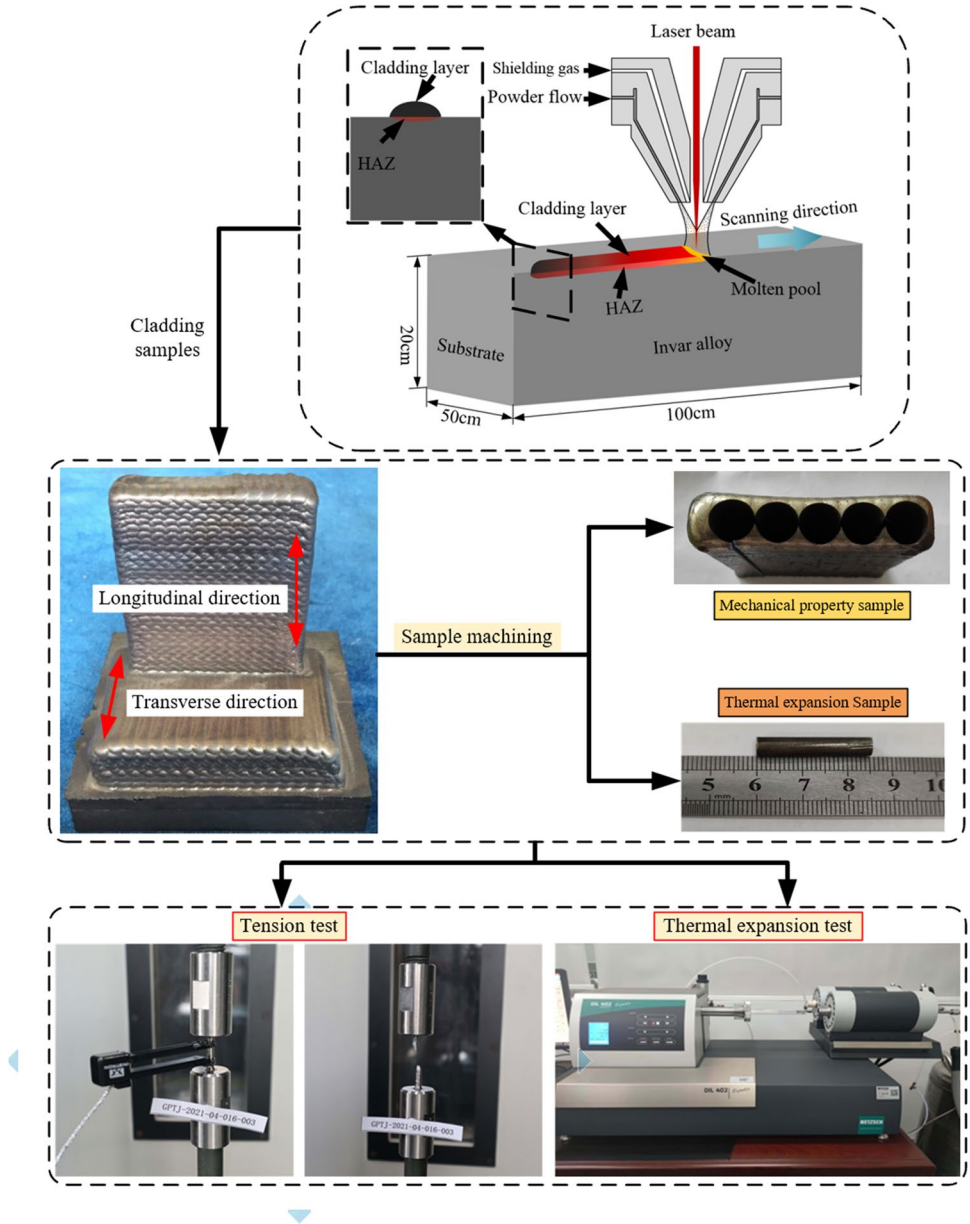


Fig. 2 Diagrammatic of laser cladding process



sample are as follows: the laser power is 1500 W, the scanning speed is 3 mm/s, and the powder feeding rate is 5 g/s. The cross sections of the cladding layers were sliced with the wire-electrode cutting and then were ground and polished through the carborundum papers with different particle sizes after the laser cladding experiments. Data on the geometrical feature of the cladding layer were obtained using a non-contact optical profiler (Sensofar, Spain) that uses the white light interferometry to extract the width, height, and cross-sectional profile of the cladding layer. The microstructure of the cladding layer was analysed by a Leica DMILM metallographic microscope (Leica, Germany).

The fracture of the Invar alloy laser cladding layer and substrate tensile samples was analysed using a German ZEISS SEM to observe the micro organizational characteristics of the fracture, supplemented by qualitative and quantitative analysis of the micro-region composition with X-ray EDS to further analyse the fracture mechanism and nature of the sample, which can be used to judge the mechanical performance of the cladding layer, and to be as a basis for improving the parameters of the laser cladding process.

The coefficient of thermal expansion of laser cladding layers of the Invar alloy was determined using a NETZSCH DIL 402 Inductive Thermal Expansion Meter from Germany. Before the test started, one end of the thermal expansion sample was fixed on the sample baffle, and the core of the inductance displacement meter was connected to the other end of the test rod, which was connected to the core of the inductive displacement meter. The measurement temperature range of this test was 20–205 °C, with a temperature change rate of 5 K/min, and the flow rate of protective gas argon was 40 mL/min. After setting the parameters, the test started. As the temperature rose, the data in the inductive displacement meter was recorded and the linear thermal expansion curve was obtained.

2.3 Experimental procedures

(1) Preparation of tensile samples

In this paper, multi-pass and multi-layer was used to obtain cladding layers in two different directions, transverse

and longitudinal. In order to ensure the rigor of the test and comprehensively analyse the mechanical properties of the cladding layer, three tensile samples were taken from the cladding layers in two different cladding directions, and two tensile samples were taken on the substrate to compare the mechanical properties of the cladding layer between layers and along the cladding direction with that of the substrate.

After the preparation of the cladding layer was completed, the two cladding layers in different directions were separated from the substrate by wire cutting, and then, the cladding layer and the substrate were sanded and polished using a grinder to remove the oxide film and impurities on the surface. After the grinding and polishing treatment, three $\phi 8 \text{ mm} \times 45 \text{ mm}$ cylinders were wire-cut on each of the two different directions of the cladding layers, and two $\phi 8 \text{ mm} \times 45 \text{ mm}$ cylinders were wire-cut on the substrate. The wire-cut samples were put into a CNC machine for machining to obtain a total of 8 tensile samples. Then, the sandpaper was used to smooth both ends of the processed tensile sample and wash the oil and impurities, the size of the tensile sample is shown in Fig. 3a, and the tensile sample is shown in Fig. 3b.

The test was carried out at room temperature, and both ends of the tensile sample were fixed on the universal material testing machine using threaded clamps to ensure that the direction of tension was perpendicular to the horizontal plane. After the fixation of the tensile sample, the electronic extensometer was clamped on the sample, and the original scale distance of the extensometer was 12.50 mm. The equipment was fine-tuned to ensure that the displacement of the sample before the test was 0. After all the preparations were completed, the testing machine was started, and the loading speed was set at 2 mm/min. The test was conducted by paying attention to the change of the load–displacement curve in the computer as well as the deformation of the sample. When the sample load reached the upper yield strength, the extensometer was removed and the deformation of the sample was carefully observed to determine whether the phenomenon of necking. Then, the load was applied until the sample pulled off, as shown in Fig. 4.

The tensile samples tested were non-standard circular tensile samples, numbered from 1 to 8, where numbers 1–3 were taken from the transverse cladding, numbers 4–6 were

Fig. 3 The size of the tensile specimen

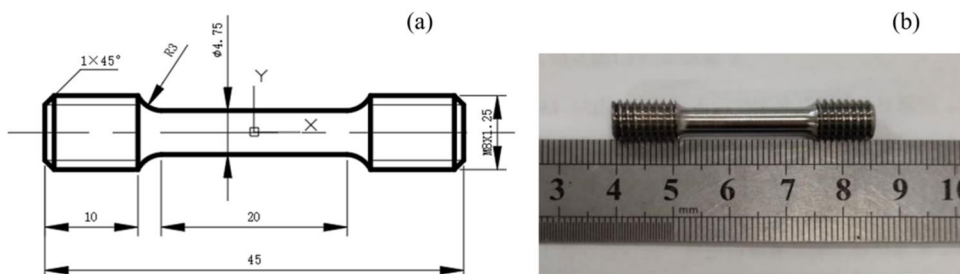


Fig. 4 Tensile specimen

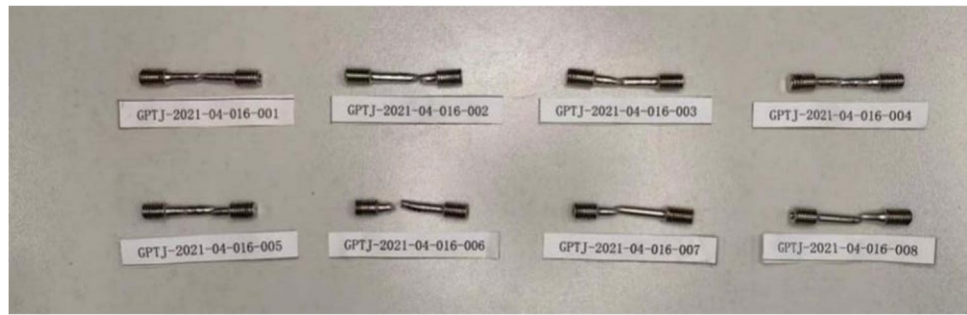


Table 3 The actual size of the tensile specimen

Sample no	Diameter (mm)			Average diameter d_0 (mm)	Initial cross-sectional area A_0 (mm ²)
	1	2	3		
1	4.76	4.76	4.77	4.76	17.81
2	4.77	4.76	4.75	4.76	17.79
3	4.76	4.77	4.77	4.77	17.84
4	4.76	4.75	4.75	4.75	17.74
5	4.75	4.76	4.77	4.76	17.79
6	4.76	4.75	4.76	4.76	17.76
7	4.76	4.76	4.76	4.76	17.79
8	4.77	4.76	4.76	4.76	17.81

Table 4 The actual size of the thermal expansion samples

Sample number	Original length of samples (mm)			Mean length L_0 (mm)
	1	2	3	
1	25.05	25.06	25.05	25.05

taken from the longitudinal cladding, and numbers 7–8 were taken from the substrate. Before testing, the dimensions of the samples were measured, and the actual dimensions of the samples are shown in Table 3.

(2) Preparation of thermal expansion sample

After the sample was polished, cut out a $\phi 6$ mm \times 25 mm cylinder on the Invar alloy cladding layer. Then, the sandpaper was used to polish the two ends of the wire-cut sample to ensure them smooth and flat, and clean the surface oil with acetone.

The thermal expansion coefficient of the Invar alloy laser cladding layer was measured by the thermal expansion performance test, and compared with the thermal expansion coefficient of the substrate to determine the effect of the laser cladding, and as a basis for improving the laser cladding process parameters. The thermal expansion sample used in the test is a standard cylindrical sample with a size of $\phi 6$

mm \times 25 mm. The actual size of the thermal expansion samples is shown in Table 4.

3 Results and discussion

3.1 Thermal expansion performance

The linear thermal expansion $\Delta L/L_0$ and temperature T data of the thermal expansion sample of the Invar alloy cladding layer were obtained from the thermal expansion test, and the linear thermal expansion curve was drawn, as shown in Figs. 4, 5, 6, 7 and 8, and the calculation formula of the linear thermal expansion $\Delta L/L_0$ is:

$$\Delta L_i/L_0 = \frac{L_i - L_0}{L_0} \tag{1}$$

where L_0 is the original length of the sample at 25 °C room temperature (mm) and L_i is the length of the sample at temperature T_i (mm).

The linear thermal expansion $\Delta L/L_0$ obtained from the thermal expansion test can be converted into the average linear expansion coefficient α_m :

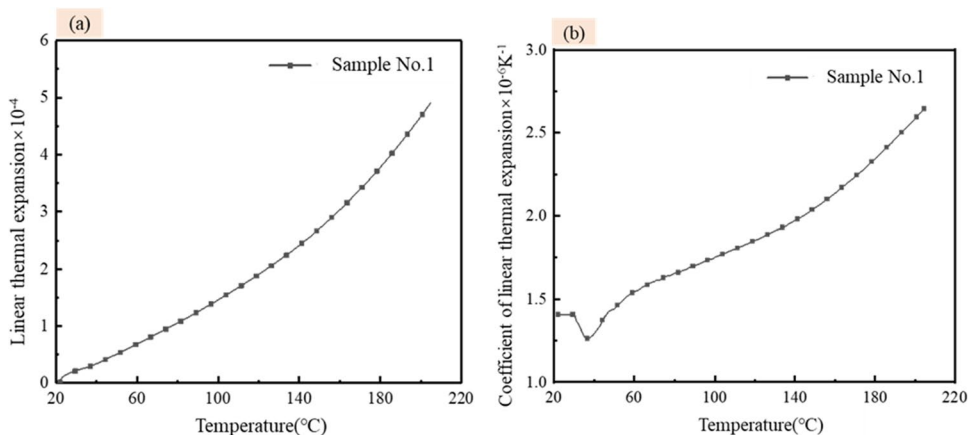
$$\alpha_m = \frac{\Delta L_i/L_0}{\Delta T} = \frac{\Delta L_i/L_0}{T_i - T_0} \tag{2}$$

where T_0 is 25 °C room temperature and α_m is the average linear expansion coefficient of the sample (the unit is generally 10^{-6} K^{-1}).

The average linear expansion coefficient α_m of the thermal expansion sample is calculated by Eq. (2), and the average linear expansion coefficient curve is shown in Fig. 5.

As can be seen from Fig. 5, the linear expansion coefficient of the cladding layer sample decreases significantly from 20 to 40 °C, showing anomalous thermal expansion characteristics similar to that of Invar alloy, and increases slowly in the temperature range of 40~200 °C. In the range of 20~200 °C, the linear expansion coefficient of the cladding layer sample is maintained at a low level (about $1.5 \times 10^{-6}/\text{K} \sim 2.6 \times 10^{-6}/\text{K}$). The average linear expansion coefficient of the Invar

Fig. 5 **a** Linear thermal expansion curve of thermal expansion sample of cladding layer. **b** Average linear expansion coefficient curve of thermal expansion sample of cladding layer



alloy and the thermal expansion sample of the cladding layer at 25–200 °C are shown in Table 5.

The linear expansion coefficient of sample 1 is basically consistent with that of the Invar alloy in the temperature range of 25–150 °C, within 5% difference, and the coefficient of linear expansion in the range of 150–200 °C is slightly larger than that of the Invar alloy, with a difference of about 10%. Therefore, a 10% difference between the thermal expansion coefficient of the cladding layer and the base metal is considered a good cladding performance, and the cladding effect of the cladding layer sample is excellent, which meets the requirements of the base metal. Thus, it concludes that the Invar alloy laser cladding layer prepared by the laser process parameters has a good thermal expansion performance that is compatible with the base metal.

3.2 Mechanical property

3.2.1 Experimental data of cladding layer and substrate

The load F and displacement ΔL data of the transverse cladding layer, longitudinal cladding layer and substrate for the 8 samples were obtained by tensile tests. The load–displacement curves of samples 1 to 8 are shown in Fig. 6a–c.

3.2.2 Analysis of mechanical properties of transverse cladding layer

The displacement variation ΔL and applied load F of the tensile sample for the Invar alloy in transverse cladding layer obtained by tensile tests can be transformed into stress σ and strain ε .

$$\sigma = \frac{F}{A_0} \quad (3)$$

$$\varepsilon = \frac{\Delta L}{L_0} \quad (4)$$

where F is the load applied on the sample (N); A_0 is the initial cross-sectional area of the sample (mm^2); L_0 is the initial gauge length of the sample (mm); ΔL is the displacement variation of the sample (mm); σ is the stress on the sample (MPa); and ε is the strain produced by the sample (mm/mm).

The initial gauge length L_0 and final gauge length after fracture L_e obtained from the extensometer can be used to calculate the percentage elongation after fracture δ of the transverse cladding layer tensile sample.

$$\delta = \frac{L_e - L_0}{L_0} \times 100\% \quad (5)$$

where L_e is the final gauge length after fracture of the sample (mm) and δ is the percentage elongation after fracture (%).

The stress and strain of the transverse cladding layer sample are derived from Eqs. (3) and (4), and the stress–strain curve of the transverse cladding layer sample based on the tensile test is shown in Fig. 7. The percentage elongation after fracture of the transverse cladding layer sample δ is calculated by Eq. (5), as shown in Table 6.

Figure 7 shows that the stress–strain curves of the transverse cladding layer samples are basically consistent, which indicates the good uniformity of the transverse laser cladding layer for the Invar alloy, and its stress–strain curves have continuous transitions, which suggests its preferable plasticity. Taking sample 1 as an illustration, the strain–stress curve of the sample is roughly straight during the elastic deformation stage. The material has no obvious yield stage after the elastic deformation stage. Since the time point at which the material starts to change from the elastic deformation to plastic deformation is difficult to obtain, the stress $\sigma_{p0.2}$ when the plastic strain of the sample is 0.2% is taken as the yield strength σ_s of the sample, which is about 267 MPa. During the hardening

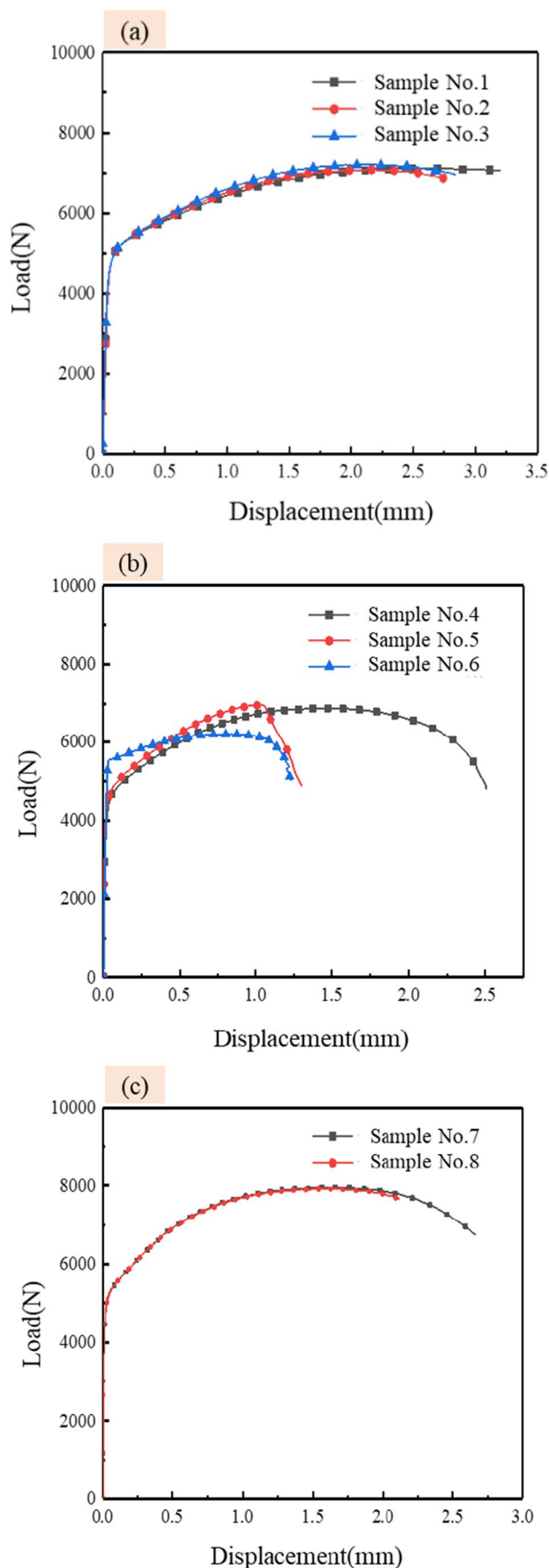
Fig. 6 **a** Load–displacement curve of the transverse cladding layer, **b** load–displacement curve of the longitudinal cladding layer, and **c** load–displacement curve of tensile specimen of substrate

stage, the stress and strain of the sample continue to increase, and the maximum stress of the sample is taken as the tensile strength σ_b of the material, which is about 399 MPa. In the local deformation and fracture stage, the stress–strain curve of the material decreases rapidly after passing through the highest point. The sample began to show necking phenomenon until the sample was broken, and the tensile test was completed. Based on the final gauge length after fracture measured, it can be calculated that the elongation after fracture δ for sample 1 is 46.56%, which has a good plastic tenacity.

3.2.3 Analysis of mechanical properties of longitudinal cladding layer

The stress and strain of the Invar alloy longitudinal cladding layer sample are derived from Eqs. (3) and (4), and the stress–strain curve of the longitudinal cladding layer sample is shown in Fig. 8. The percentage elongation after fracture δ of the longitudinal cladding layer sample is calculated from Eq. (5), as shown in Table 7.

Figure 8 shows that the stress–strain curve of the longitudinal cladding layer sample fluctuates greatly, which indicates the inhomogeneity of the mechanical properties of the Invar alloy longitudinal cladding layer. Samples 4 and 5 have comparable stress–strain curves and the corresponding similar mechanical characteristics. The stress–strain curve of sample 4 shows a continuous transition, comparing to that of the transverse cladding layer, indicating that its plasticity is also good. The stress–strain curve of sample 6 fluctuates significantly, and at the peak of the curve and the fracture of the sample, the strain is small, which indicates the small tensile strength and poor plasticity, and the poor comprehensive mechanical properties of sample 6. Taking samples 4 and 6 as an example, the yield strength σ_s and tensile strength σ_b of sample 4 are about 255 MPa and 388 MPa respectively. The yield strength σ_s and tensile strength σ_b of sample 6 are about 313 MPa and 350 MPa respectively. The tensile strength of sample 6 is 9.8% lower than that of sample 4 and 12.3% lower than that of the transverse cladding layer sample 1. The calculated elongation δ of sample 4 is 43.36%, and that of sample 6 is 35.92%. No significant difference was observed between the percentage elongation after fracture of samples 4 and 1; however, the small percentage elongation of sample 6 indicates that the plasticity of the longitudinal cladding layer is relatively poor.



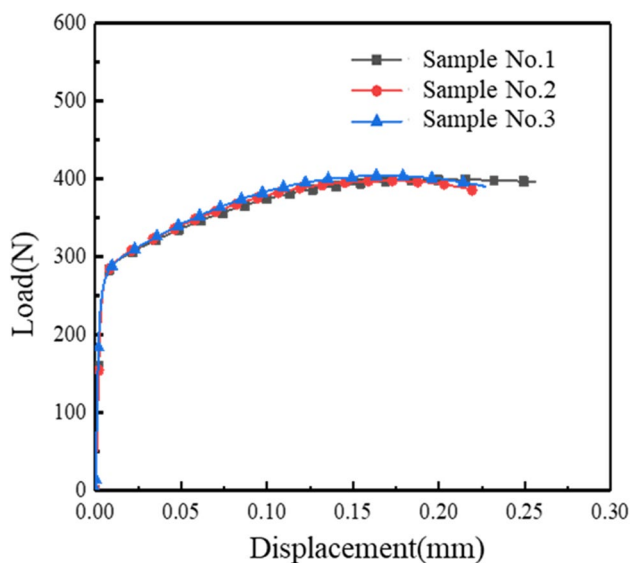


Fig. 7 Stress–strain curve of the transverse cladding tensile specimen

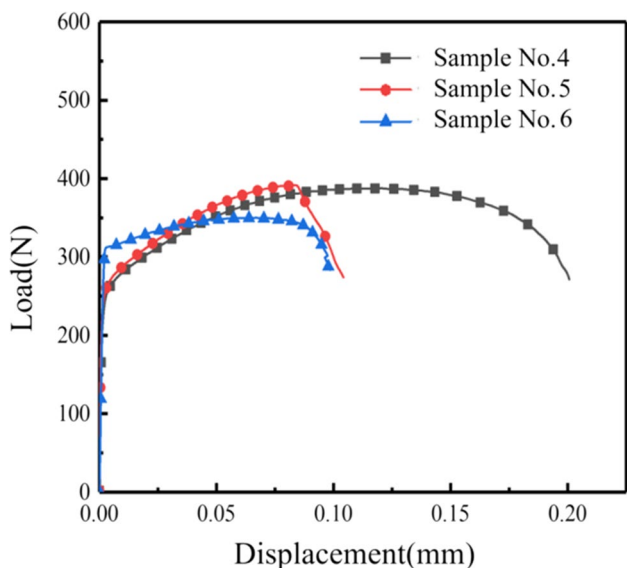


Fig. 8 Stress–strain curve of the longitudinal clad tensile specimen

Table 5 The average linear expansion coefficient of the Invar alloy and the thermal expansion sample of the cladding layer ($10^{-6}/K$)

Temperature (°C)	25–50	50–100	100–150	150–200
Sample 1	1.44	1.75	2.05	2.59
Invar alloy	1.5	1.7	2.0	2.35
Error%	4	2.9	2.5	10.2

Table 6 The percentage elongation after fracture of the transverse cladding layer sample

Order number	Initial gauge length L_0 (mm)	Final gauge length after fracture L_e (mm)	Percentage elongation after fracture δ (%)
Sample 1	12.50	18.32	46.56
Sample 2	12.50	17.51	40.08
Sample 3	12.50	18.72	49.76

Table 7 The percentage elongation after fracture of longitudinal cladding layer sample

Order number	Initial gauge length L_0 (mm)	Final gauge length after fracture L_e (mm)	Percentage elongation after fracture δ (%)
Sample 4	12.50	17.92	43.36
Sample 5	12.50	17.84	42.72
Sample 6	12.50	16.99	35.92

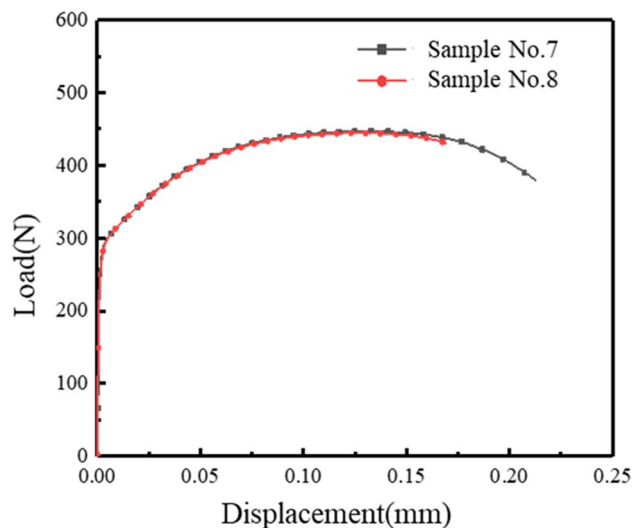


Fig. 9 Stress–strain curve of the tensile specimen of substrate

Table 8 The percentage elongation after fracture of the substrate sample

Order number	Initial gauge length L_0 (mm)	Final gauge length after fracture L_e (mm)	Percentage elongation after fracture δ (%)
Sample 7	12.50	18.22	45.76
Sample 8	12.50	18.16	45.28

3.2.4 Mechanical properties of substrate

The stress and strain of the Invar alloy substrate sample are derived from Eqs. (3) and (4), and the stress–strain curve of

the substrate sample is shown in Fig. 9. The percentage elongation after fracture δ of the substrate sample was calculated by Eq. (5), as shown in Table 8.

As shown in Fig. 9, the stress–strain curves of the two samples basically coincide, showing the Invar alloy substrate material's uniformity, and its stress–strain curve transitions continuously, indicating its good plasticity. Taking sample 7 as an example, the yield strength σ_s and tensile strength σ_b are about 288 MPa and 447 MPa respectively, and the tensile strength is higher than that of the transverse cladding and longitudinal cladding layers. The percentage elongation after fracture δ is 45.76%, which is similar to that of the transverse cladding layer and higher than that of the longitudinal cladding layer. This indicates that the plasticity of the transverse cladding layer is similar to that of the base metal, and the plasticity of the longitudinal cladding layer is poor.

3.2.5 Comparison of mechanical properties of cladding layer and substrate

The mechanical property parameters of the tensile samples obtained by the tensile test are shown in Table 9. According to the data from the table, the following conclusions can be drawn: the comprehensive mechanical properties of the transverse cladding layer, i.e., the cladding layer along the cladding direction, are similar to those of the base metal, and the average tensile strength is about 10.2% lower than that of the base metal. The percentage elongation of samples 1 and 3 increased by 1.7% and 8.7% respectively by comparing with the base metal, that of sample 2 decreasing by 12.6% in comparison with the base metal, and the plastic tenacity is not much different from that of the base metal. The longitudinal cladding layer, i.e., the mechanical properties between the cladding layers, is unevenly distributed, and the tensile strength is greatly different. The tensile strength of samples 4 and 5 was reduced by about 12.5%, and the percentage elongation after fracture was reduced by about 6.5% by comparing with the parent material, and the comprehensive

mechanical properties are slightly lower than that of the base metal. The tensile strength and the percentage elongation after fracture of sample 6 was respectively 21.4% and 21.6% lower than those of the base metal, showing its poor comprehensive mechanical properties. The results show that the comprehensive mechanical properties of the Invar alloy cladding layer along the cladding direction are better, and the comprehensive mechanical properties between layers are poor.

3.3 Fracture analysis

In this part, the fracture characteristics and microstructure of 8 tensile samples were observed and analysed by SEM. The working voltage of SEM was 20 kV, and the probe was SE1 probe (secondary electron imaging directly excited by incident electrons), to take localized magnified images of macroscopic fracture at low magnification (25 ~ 35 \times), 200, 500, 1000, 1500 and other magnifications of the fracture.

3.3.1 SEM analysis of substrate sample fracture

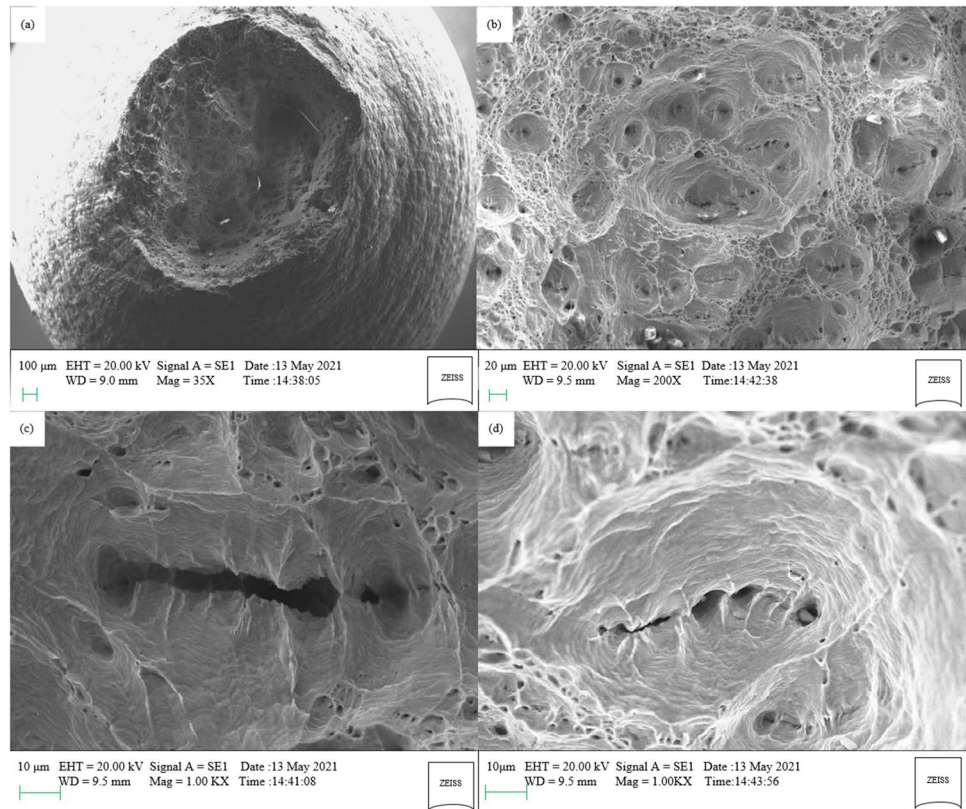
The macroscopic fracture morphology and local microstructure magnification characteristics of the substrate sample 7 are shown in Fig. 10. As can be seen in Fig. 10a, the macroscopic fracture morphology of sample 7 shows a relatively regular circular shape with obvious necking process, the boundary between the radiation zone and the shear lip is obvious, and the inclination angle between the outer edge of the fracture and the axis is about 45°, which is a typical cup-cone fracture morphology. Figure 10b shows the fibre area of the fracture, which is relatively smooth and flat, showing more microvoid coalescence. The phenomenon of microvoid coalescence is the dimple pattern in the fracture. The stress concentration is caused by the brittle phases such as the second phase particles or inclusion particles in the material, which is a unique phenomenon in the fracture of plastic materials. The more the number of dimples, the deeper the depth and the larger the size, the better the plastic tenacity of the material. It can be seen that the fracture property of sample 7 is a dimple-type ductile fracture nucleated in the fibre zone, with good plasticity, which is also consistent with the percentage elongation after fracture parameter obtained by the tensile test. The partial enlarged views of the fracture fibre zone in Fig. 10c, d show that there are some long strip cracks on the fracture surface, which is due to the aggregation and growth of the micropores inside the material during tension, and finally, the crack propagation is formed.

The macroscopic fracture morphology and local microstructure magnification characteristics of substrate sample 8 are shown in Fig. 11. As can be seen in Fig. 11a, the macroscopic fracture morphology of sample 8 shows a regular circular shape, the boundary between the radiation zone and

Table 9 Mechanical properties parameters of tensile samples

Sample number	Yield strength σ_s (MPa)	Tensile strength σ_b (MPa)	Percentage elongation after fracture δ (%)
1	267.4	398.8	46.6
2	268.5	397.6	40.0
3	261.7	404.1	49.8
4	255.3	387.9	43.4
5	260.6	391.5	42.7
6	312.9	349.9	35.9
7	287.6	446.9	45.8
8	285.6	444.6	45.3

Fig. 10 SEM fracture characteristics of sample 7



the shear lip is obvious, the shear lip is smooth and uniform, and the angle with the axis is 45° . The fracture fibre zones in Fig. 11b, c show more dimple patterns, indicating the good plastic tenacity of the material, and the fracture property is dimple-type ductile fracture nucleated in the fibre zone. Figure 11d–f are the fracture radiation areas, showing a large number of pores, pits and cracks. Figure 11e shows the crack caused by the second phase particles, and the crack propagates along the oblique 45° direction.

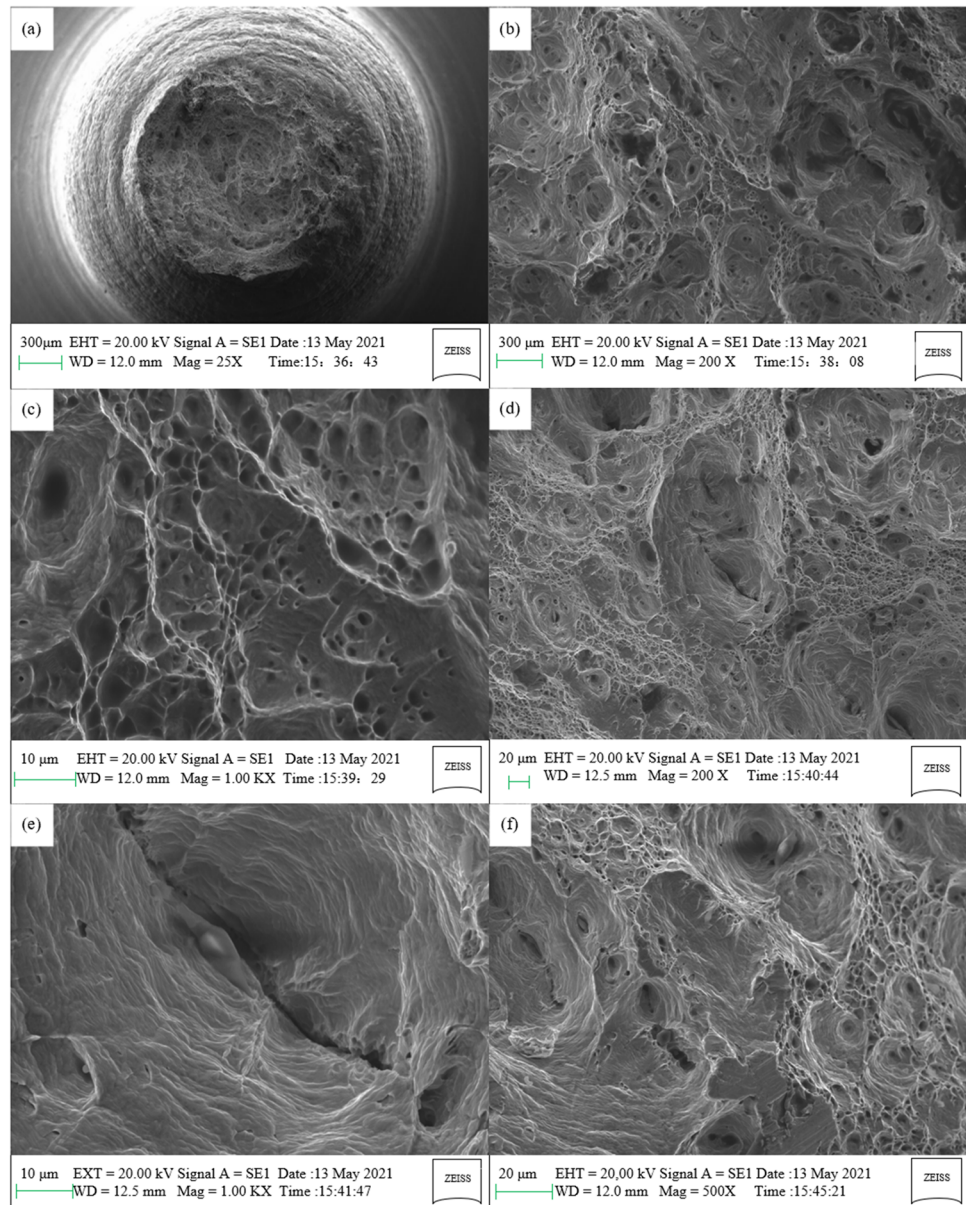
As shown in Figs. 10 and 11, the fracture of the Invar alloy substrate sample is a regular cup-cone fracture, whose surface is smooth and uniform. The boundary between the radiation zone and the shear lip zone is obvious, and the fracture fibre zone has more dimple patterns. The fracture property is a dimple-type ductile fracture nucleated in the fibre zone, with a good plastic tenacity. The percentage elongation after fracture of the base metal obtained by the tensile test is about 45%. The fracture morphology of the substrate sample is consistent with the tensile test results.

3.3.2 SEM analysis of fracture of transverse cladding layer

The macroscopic fracture morphology and local microstructure magnification characteristics of the transverse cladding layer sample 1 are shown in Fig. 12. From Fig. 12a, it can be observed that the macroscopic fracture of sample 1 shows an irregular shape without obvious radial zones, the shear lip is

duller and rougher compared with that of the substrate sample, the angle with the axis is not a regular 45° , and there are many hole-like structures on the fracture surface. It can be observed from Fig. 12b–d for the fracture of the fibre zone that more equiaxial ligamentous fossa and tearing ligamentous fossa are found, which indicates the good plasticity of the material, the nature of the fracture for the ligamentous fossa-type tenacity of the fibre zone-shaped nuclei of the fracture. From the tensile test, it can be obtained that the percentage elongation after fracture of sample 1 is 45.56%, which is the same as the parent material, and the electron microscopy analysis and tensile test results are in line with the results. Meanwhile, some larger and deeper craters were observed in Fig. 12b, c, which may be due to the pore defects caused by the internal inclusions or the second brittle phase of the material, resulting in a reduction of its tensile strength compared with the substrate.

The macroscopic fracture morphology and local microstructure magnification characteristics of the transverse cladding layer sample 2 are shown in Fig. 13. From Fig. 13a, it can be observed that the macroscopic fracture of sample 2 shows an irregular shape, the fracture surface is rough and uneven and there are many pores, there is no obvious radial zone, and the boundaries between the shear lip area and the fibre area are not obvious, with the angle between the shear lip and the axis less than 45° , and the fracture area has a larger proportion of the shear lip, which indicates that the

Fig. 11 SEM fracture characteristics of sample 8

material's tenacity is poor. Figure 13b for the fracture of the shear lip area and the outer edge of the radial zone, it can be seen that the shear lip appears to be part of the step pattern, which is the characteristic of quasi-dissolution fracture, and it belongs to the brittle fracture. The quasi-dissolution fracture is caused by the existence of voids within the grain, inclusions and the second phase of the plasmonic point. Figure 13c, d show the fracture of the fibre area; it can be seen in the fibre area that there are a large number of tough nest-like patterns, the nature of the fracture for the tough nest tenacity fracture, but at the same time in the fibre area, there is also a large pit, which may be the material internal inclusions or the existence of the second brittle phase caused by the material plastic tenacity reduction. The tensile test results show that the percentage elongation after

fracture of sample 2 is about 40%, and the tensile strength is 397 MPa, both of which are slightly lower than that of the parent material, which is consistent with the results of the electron microscope analysis.

The macroscopic fracture morphology and local microstructure magnification characteristics of the transverse cladding layer sample 3 are shown in Fig. 14. From Fig. 14a, it can be observed that the macroscopic fracture of sample 3 is a regular cup-and-conical fracture, with uneven fracture surface, less porous, and the boundary between the shear lip area and the radiation area is not obvious. The angle between the shear lip and the axis is about 45° , with small proportion of the fracture accounted for by the shear lip, and the proportion of the radiation area and the fibre area is larger, indicating that the material's plasticity is good. Figure 14b,

Fig. 12 SEM fracture characteristics of sample 1

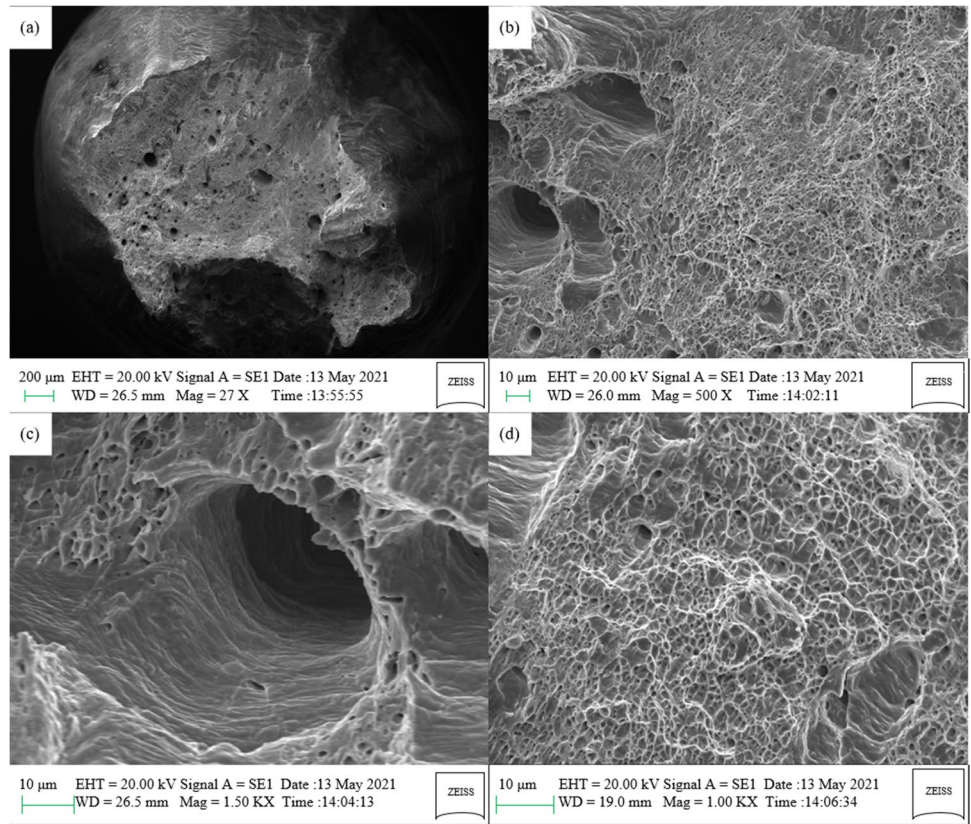


Fig. 13 SEM fracture characteristics of sample 2

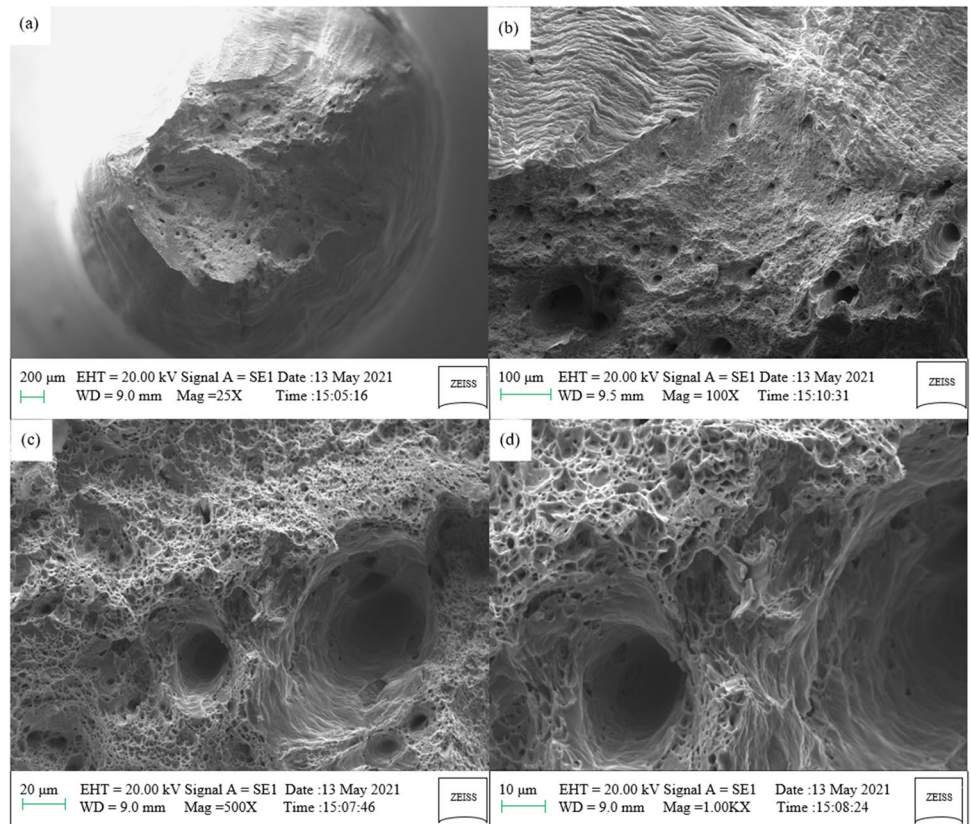
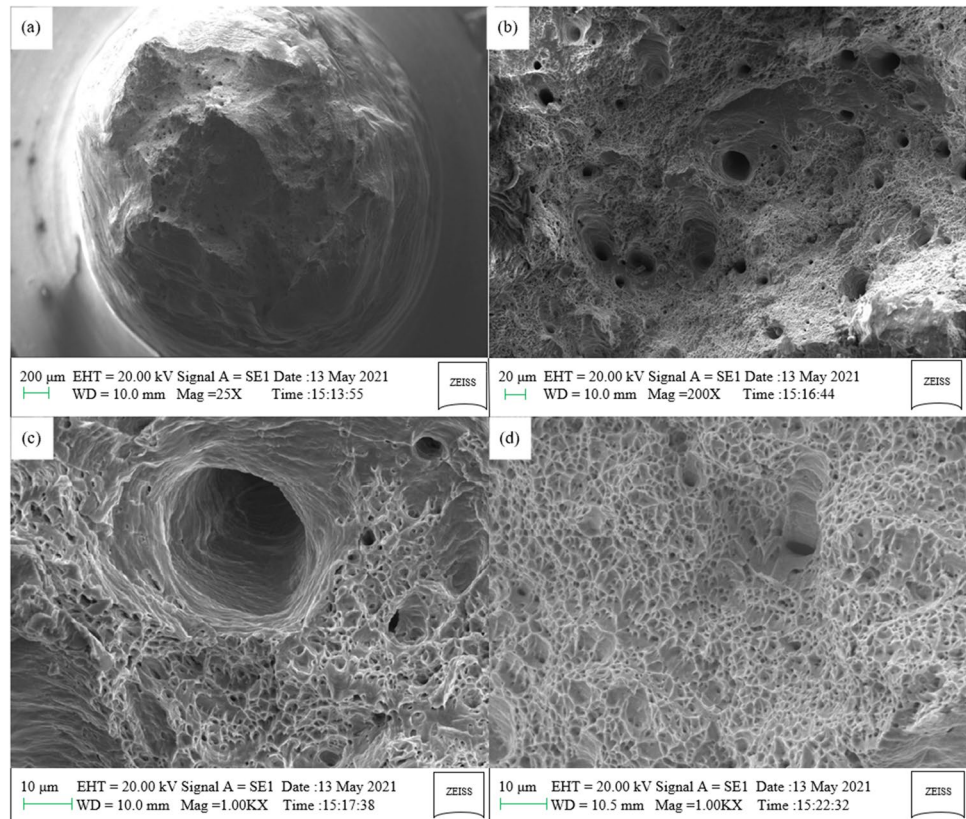


Fig. 14 SEM fracture characteristics of sample 3

c show the fracture of the radioactive area, from which can be seen in the radioactive area that there are more large and deep holes and easy-to-produce microcracks, reducing the plastic tenacity of the material. At the same time, the radial zone also appears as part of the tough nest-like pattern, with better plasticity. Figure 14d for the fracture of the fibre area, from which can be seen in the fibre area that there are a large number of equiaxial tough fossa, the nature of the fracture for the fibre area of the shape of the nucleus of the tough fossa tenacity of the fracture, large and deep pits and pores less, and the material's plastic tenacity is good. Tensile test results show that the percentage elongation after fracture of sample 3 is 49.8%, the plasticity is improved compared with the parent material, and the tensile strength is higher than that of samples 1 and 2, which are consistent with the fracture characteristics.

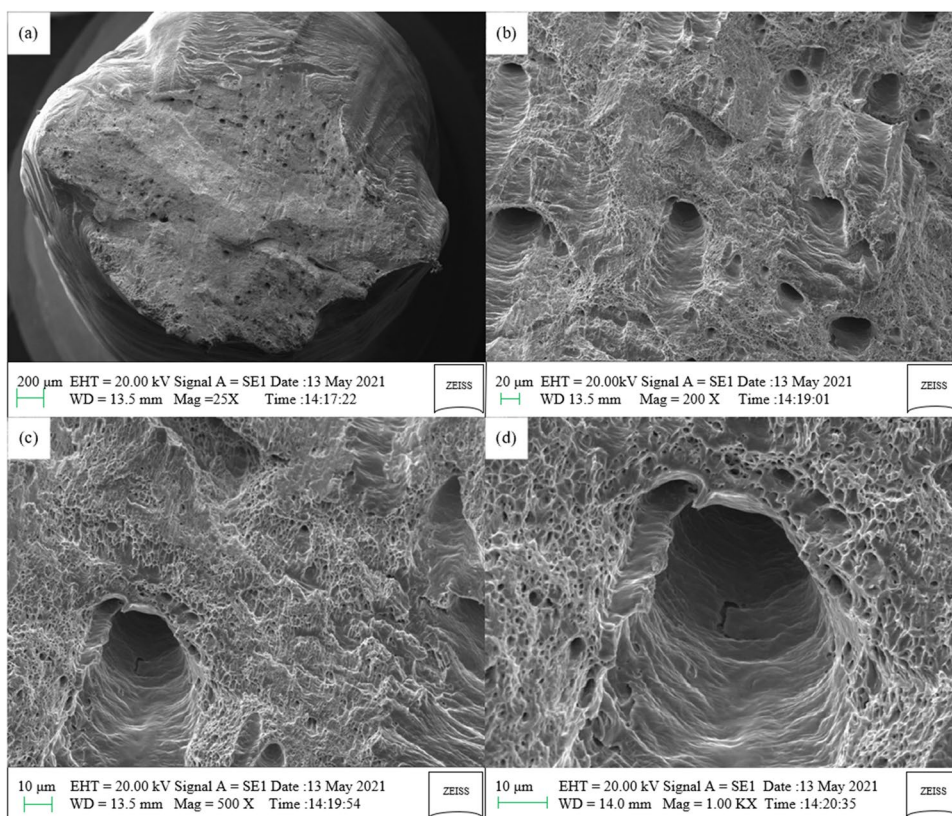
As seen from Figs. 12, 13, and 14, the macroscopic fracture of the Invar alloy transverse cladding layer samples shows a more irregular shape than that of the substrate, with a rougher surface and no obvious radial zone. The fibre areas have more tough nest-like patterns, the fractured nature of the fibre area nucleus tough nest tenacity fracture, with better plastic tenacity, which are consistent with the parent material. However, at the same time, the fibre zone and the radiation zone have more porosity, which may be due to the presence of impurities and the second brittle phase which

makes the tensile strength of the cladding layer reduced compared with the substrate.

3.3.3 SEM analysis of fracture of longitudinal cladding layer

The macroscopic fracture morphology and local microstructure magnification characteristics of the longitudinal cladding layer sample 4 are shown in Fig. 15. From Fig. 15a, it can be observed that the macroscopic fracture of sample 4 is more irregular, without an obvious necking process, the boundaries of the fibre zone, radial zone, and shear lip zone are not obvious, and the fracture surface is flat with more pores. Figure 15b–d show the fracture of the fibre area; it can be seen on the surface of the fibre area that there are a large number of shrinkage holes, which has produced obvious microcracks, and there are a small number of step-like pattern, belonging to the quasi-dissociative brittle fracture. Also, it presents part of the ridge-like pattern, the fractured nature of brittle along the crystalline fracture phenomenon, the formation of the cause of the brittle phase precipitation caused by the grain boundary embrittlement cracking, and the plastic tenacity is poor. Figure 15c, d show that the fibre area also exists a tough nest-like pattern, but the size of the tough nest with the parent material is relatively small compared with shallow, poor plasticity. Figure 15d shows the

Fig. 15 SEM fracture characteristics of sample 4

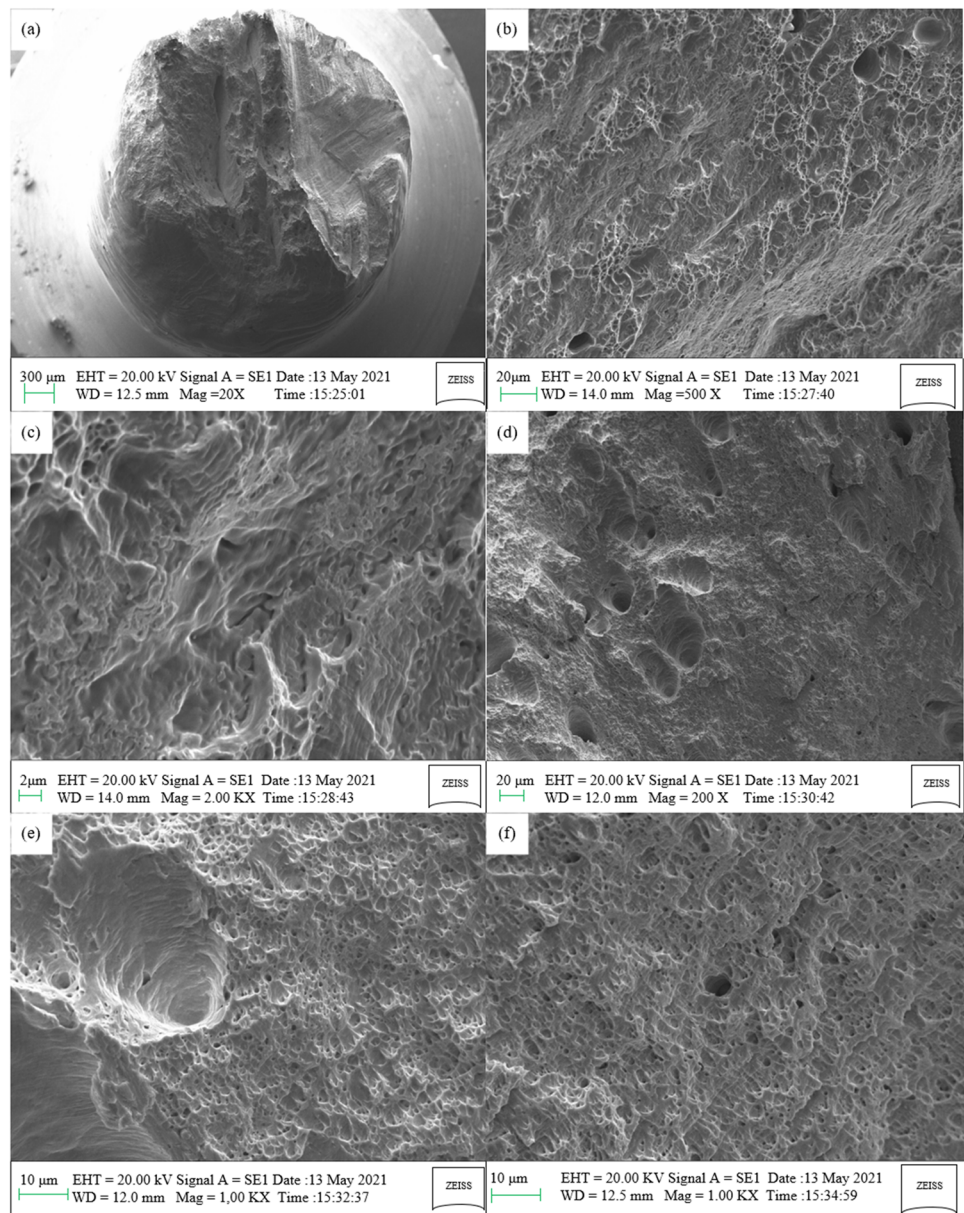


pore defects in the fibre region, which may be due to internal voids, impurities and second-phase particles, within the material and make the plastic tenacity of the material lower. The tensile test results show that the tensile strength and the percentage elongation after fracture of sample 4 are lower than those of the substrate and transverse cladding samples, which is consistent with the fracture characteristics.

The macroscopic fracture morphology and local microstructure magnification characteristics of the longitudinal cladding layer sample 5 are shown in Fig. 16. From Fig. 16a, it can be observed that the macroscopic fracture shape of sample 5 is irregular, without an obvious necking process. The surface is rough and uneven, sharp and less porous, and the boundary between the fibre area and the radiation area is not obvious, with smoother and shinier shear lip, at an angle of 45° with the axis. From Fig. 16b, c, it can be observed in the fracture fibre area that there are many stone-like patterns and tearing prongs, the fractured nature of the microporous type along the crystal fracture, the formation of this phenomenon is caused by brittle phase precipitation due to the damage to the grain boundaries, but the grain boundaries still have a certain degree of plastic deformation; for a certain degree of transition to plastic deformation after the emergence of brittle fracture, plastic tenacity is not good. From Fig. 16d, e, it can be observed in the fibre area that there are some not deep pit porosity and more tough nest-like pattern, the nature of the fracture for the tough nest tenacity fracture,

and the material's plasticity is better. Figure 16f shows the fibre area in the porosity, and the formation of the reason may be the second phase of the particle or impurities caused by the stress concentration. Therefore, the fracture of sample 5 has both plastic fracture and fracture along the crystal, and the plastic tenacity is poorer compared with the substrate. The tensile test results show that the tensile strength and the percentage elongation after fracture of sample 5 are lower than those of the base material and slightly lower than those of the transverse cladding sample; however, it is slightly higher than that of the longitudinal cladding sample 4, which is consistent with the fracture characteristics.

The macroscopic fracture morphology and local microstructure magnification characteristics of the longitudinal cladding layer sample 6 are shown in Fig. 17. From Fig. 17a, it can be observed that the macroscopic fracture shape of sample 6 is irregular, without an obvious necking process, the surface is rough and uneven with more pores, and the boundary between the fibre zone and the radiation zone is not obvious. Figure 17b shows that there are a large number of pits and pore defects of large size in the radial zone of the fracture, and there are also a large number of step patterns, ridge patterns and tear ribs around the pores. The fracture nature is quasi-dissociative fracture and fracture along the crystal, which is a brittle fracture, and the plastic tenacity of the material is poor. From Fig. 17c, it can be seen in the fibre area that there are obvious tough nest-like patterns,

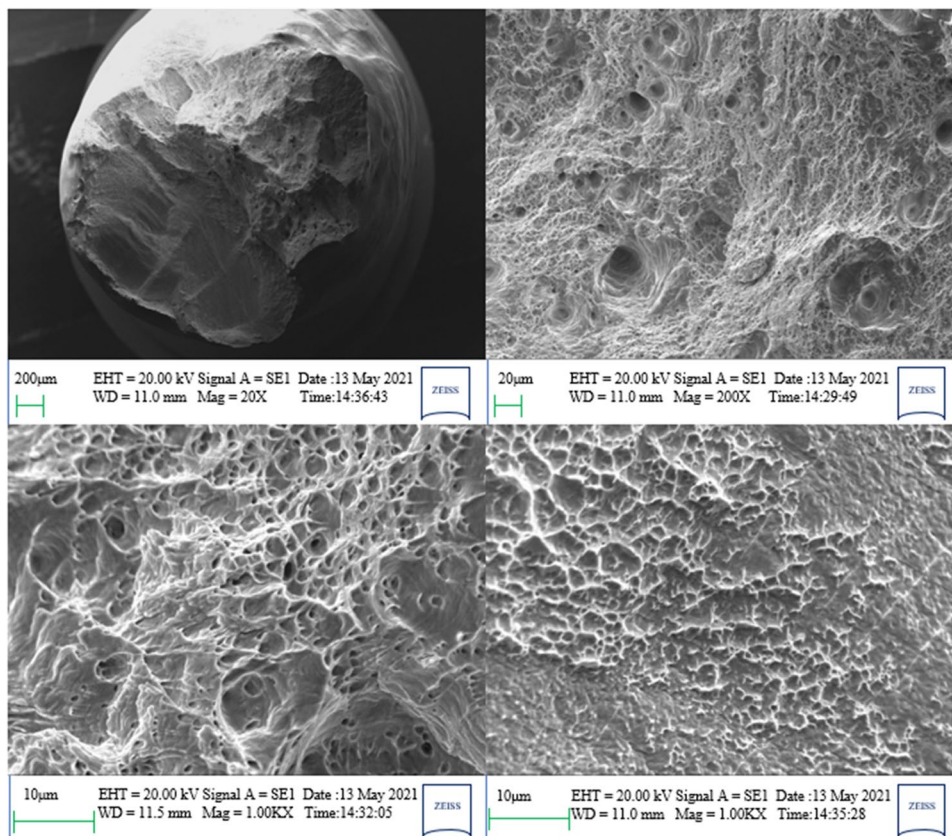
Fig. 16 SEM fracture characteristics of sample 5

the fracture nature of the tough nest type tenacity fracture, but the tough nest pattern is small, shallow and discontinuous, with poor plastic tenacity. Figure 17d show that in the fibre area, there are many continuous river-like patterns, the fractured nature of the deconvolution fracture belongs to the brittle fracture, and the plastic tenacity is poor. The formation of the brittle phase precipitation leads to the reduction of the grain boundary energy and thus triggered brittle fracture. Therefore, the simultaneous existence of disintegration fracture, quasi-disintegration fracture, fracture along the grain and tough nest fracture phenomenon in the fibre area and radial area of sample 6 indicates that the internal composition of the material is not uniformly distributed, and there is a large number of the second-phase plasmas and

impurities, which leads to the concentration of local stresses and poor plastic tenacity. Tensile test results show that the tensile strength of sample 6 is 350 MPa, and the percentage elongation after fracture is 35.9%, which are much lower than that of the substrate sample and the transverse cladding sample, and lower than the longitudinal cladding samples 4 and 5, and plastic tenacity is poor, which is consistent with the fracture characteristics.

From Figs. 15, 16, and 17, the macroscopic fracture shape of the Invar alloy longitudinal cladding layer samples is irregular, without obvious necking phenomenon and obvious boundary between the fibre zone, radial zone, and shear lip zone, and the fracture surface is rough with many shrinkage defects. For the fracture fibre area and radiation area at

Fig. 17 SEM fracture characteristics of sample 6



the same time, they are along the crystal fracture, quasi-dissolution fracture and tenacity of the nest-type fracture phenomenon. The plastic tenacity of the material is reduced comparing to the substrate and the transverse cladding layer. Also, the phenomenon of the dissolution fracture is observed in the fracture of sample 6, with poorer plastic tenacity, which may be due to the presence of more impurities in the material and the precipitation of brittle phases, resulting in the damage of the grain boundaries to cause brittle fractures, and the reduced the plastic tenacity of the material.

In summary, in the Invar alloy base plate sample fracture fibre area, there are many ligamentous nest-like patterns, the nature of the fracture for the fibre area of the nucleus of the ligamentous nest tenacity fracture, and plastic tenacity is good; in the Invar alloy transverse melting cladding layer sample fracture fibre area, there are more ligamentous nest-like pattern, the nature of the fracture for the fibre area of the nucleus of the ligamentous nest tenacity fracture. Ligamentous nest size is relatively small compared with the substrate, indicating that the plastic tenacity of the cladding layer along the melting direction is better, however, the plastic tenacity is slightly reduced compared with the substrate; in the Invar alloy longitudinal cladding layer sample fracture fibre area and radiation area at the same time, they are along the crystal fracture, quasi-dissolution fracture, and tenacity of the nest-type fracture phenomenon; for sample 6, there is a

phenomenon of dissolution fracture, indicating that there are more impurities and brittle phases inside the material; the cladding layer and the plastic tenacity of the layer between the layers are poor.

3.4 Fracture EDS analysis

In order to further qualitative and quantitative analysis of the microstructure and composition of the cladding layer and substrate sample fracture, this part of the test used an X-ray energy spectrum analyser (EDS) to analyse the composition of the fracture micro-zone organization and the elemental percentage of the fracture, and a total of five sampling points (L1~L5) were taken from samples 3, 4, and 8 as shown in Figs. 18, 19, 20, 21 and 22.

The fractured micro-area composition is shown in Table 10. The Fe content in the L1 area of sample 8 is 65.72 wt.%, which is higher than the theoretical content of 63 wt.% of the base material, the Ni content is 32.13 wt.%, which is lower than the theoretical content of 35.92 wt.% of the base material, and the C content is 2.14%, which is higher than the theoretical content of 0.20 wt.% of the base material, which suggests the precipitation of the second brittle in the L1 area. This indicates that the second brittle phase precipitated in the L1 zone is a small number of Fe–C compounds as well as free C, where the

Fig. 18 EDS analysis of fracture in L1 zone (sample 8). **a** Sampling location and **b** microanalysis

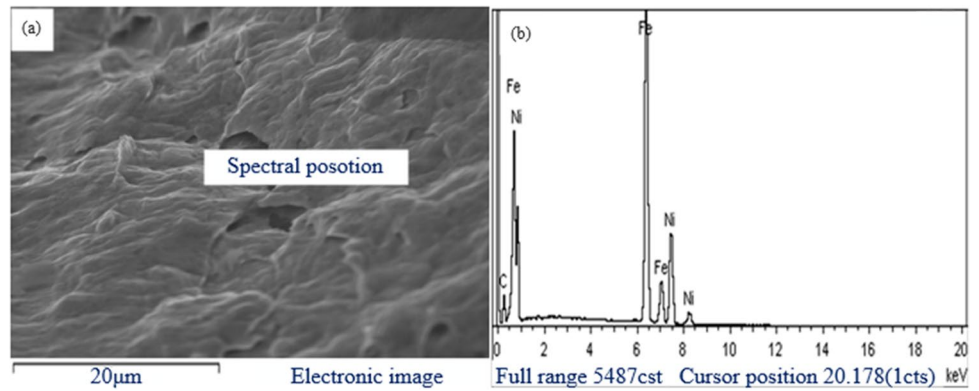


Fig. 19 EDS analysis of fracture in L2 zone (sample 8). **a** Sampling location and **b** microanalysis

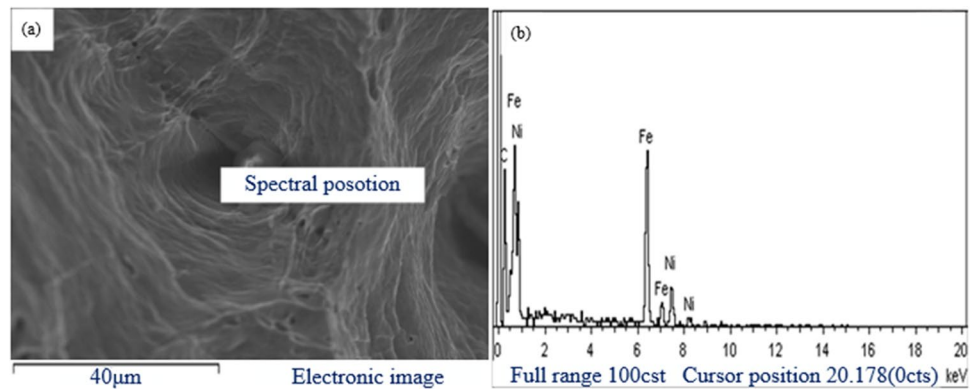
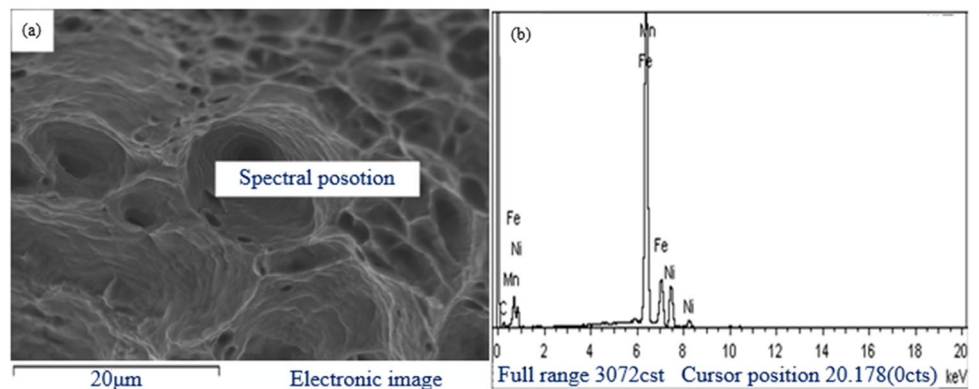


Fig. 20 EDS analysis of fracture in L3 zone (sample 8). **a** Sampling location and **b** microanalysis



stress concentration occurs, and pore defects are formed. The content of Fe in the L2 zone of sample 8 is 62.25 wt.%, which is slightly lower than the theoretical value, the content of Ni is 20.84 wt.%, which is lower than the theoretical value, and the content of C is 16.90 wt.%, which is much higher than the theoretical value, which indicates that the second brittle phase precipitated in the L2 zone is a C inclusion, which is brittle, and there is a concentration of stress in this zone, forming brittle crack extension. Sample 8 of the L3 area in the Fe content of 80.38 wt.% is much higher than the theoretical value, Ni

content of 18.39 wt.%, much lower than the theoretical value, the C content of 0.45 wt.%, slightly higher than the theoretical value, the Mn content of 0.79 wt.%, higher than the theoretical value of 0.27 wt.%, which indicates the precipitation of the second phase in the L3 area of the nickel-poor Fe–Ni phase, and a small number of Mn aggregation, where the tough nest nucleation, tenacity fracture. The Fe content in the L4 zone of sample 3 is 87.56 wt.%, much higher than the theoretical value, and the Ni content is 12.44 wt.%, much lower than the theoretical value, which indicates that the second phase

Fig. 21 EDS analysis of fracture in L4 zone (sample 3). **a** Sampling location and **b** microanalysis

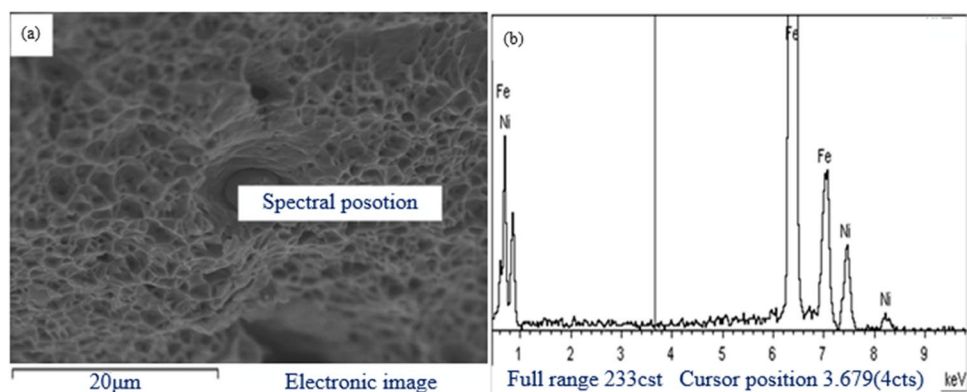


Fig. 22 EDS analysis of fracture in L5 zone (sample 4). **a** Sampling location and **b** microanalysis

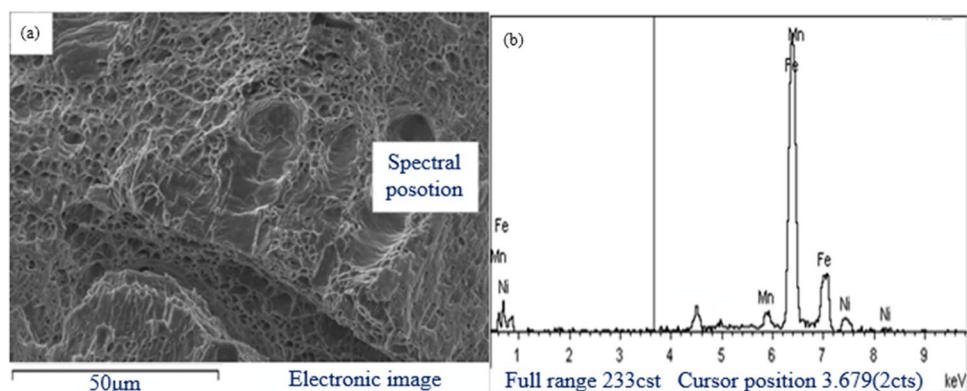


Table 10 Microcomponent of fracture

Sampling location	Fe		Ni		C		Mn		Ti	
	wt.%	at.%	wt.%	at.%	wt.%	at.%	wt.%	at.%	wt.%	at.%
L1	65.72	61.86	32.13	28.77	2.14	9.37	—	—	—	—
L2	62.25	38.74	20.84	12.34	16.90	48.92	—	—	—	—
L3	80.38	79.77	18.39	17.36	0.45	2.08	0.79	0.79	—	—
L4	87.56	88.09	12.44	11.91	—	—	—	—	—	—
L5	86.73	86.55	6.74	6.40	—	—	3.65	3.70	2.88	3.35

precipitated in the L4 zone is nickel-poor Fe–Ni phase, which is brittle, and there is a concentration of stress in this zone to form craters and pore defects. The Fe content in the L5 area of sample 4 is 86.73 wt.%, much higher than the theoretical value, the Ni content is 6.74 wt.%, much lower than the theoretical value, and the Mn content is 3.65 wt.%, much higher than the theoretical value, which indicates that the precipitated second phase is the nickel-poor Fe–Ni phase as well as free Fe and Mn aggregation, which is brittle, and in addition to the presence of the constituent Ti that is not present in the base material in L5, which may be a mixed impurity, so that a large pit porosity and brittle fracture along the crystal appeared here.

4 Conclusion

In this paper, the laser cladding of the Invar alloy surface was carried out using the same material powder in multi-pass and multi-layer, and the properties of laser cladding layer as well as the macroscopic morphology and microstructure characteristics of fracture were studied. The cladding layer's mechanical properties were studied by tensile test, its thermal expansion coefficient was measured by thermal dilatometer, fracture was analysed by scanning electron microscope (SEM), and its composition was analysed by X-ray energy-dispersive spectrometer (EDS). Conclusions are as follows:

1. The tensile test results show that the comprehensive mechanical properties of the Invar alloy cladding layer are lower than that of the base metal. The comprehensive mechanical properties of the transverse cladding layer (samples 1, 2 and 3) are not significantly different from those of the base metal, the tensile strength is slightly lower than that of the base metal and the plasticity is similar to that of the base metal. The mechanical properties of longitudinal cladding layers (samples 4, 5 and 6) are unevenly distributed, with the comprehensive mechanical properties of samples 4 and 5 similar to those of transverse cladding layers, and the comprehensive mechanical properties of sample 6 are poor, in terms of low strength and plasticity, and differing greatly from those of the parent material. This shows that the comprehensive mechanical properties of the cladding layer along the cladding direction are better, while those between the layers are poorer.
2. The thermal expansion test shows that the thermal expansion coefficient of the cladding layer is maintained at a very low level in the temperature range of 25 to 200 °C, with an error of no more than 20% from the base material, which indicates that the cladding layer has a good thermal expansion performance that are compatible with the base metal.
3. Fracture SEM analysis results show that in the Invar alloy base plate sample fracture fibre area, there are many ligamentous nest-like patterns, the nature of the fracture for the fibre area nucleation of the ligamentous nest tenacity fracture, and plastic tenacity is good; in the Invar alloy transverse melting cladding layer sample fracture fibre area, there are more ligamentous nest-like pattern, the nature of the fracture for the fibre area nucleation of the ligamentous nest tenacity fracture, and ligamentous nest size is smaller than the substrate comparison, showing that the plastic tenacity of the cladding layer along the melting direction is better, but the plastic tenacity is slightly reduced compared with the substrate; and in the Invar alloy longitudinal cladding layer sample fracture fibre area and radiation area at the same time, they are along the crystal fracture, quasi-dissolution fracture and tenacity of the nest-type tenacity of the fracture phenomenon, and the phenomenon of the dissolution fracture is observed in the fracture of sample 6, indicating that there are more impurities and brittle phases inside the material and the cladding layer with the layer of the plastic tenacity of the layer is poorer.
4. The results of fracture EDS analysis show that many nickel-poor Fe–Ni brittle phases and a small amount of Fe–C brittle phases precipitate along the crystalline brittle fracture, and there is a concentration of stress at these second-phase plasmas, which will form microcracks and expand when loaded, reducing the comprehen-

sive mechanical properties of the cladding layer. At the same time, Ti impurities are also found in some of the pore defects, which will lead to the formation of brittle fractures along the crystal, affecting the quality of the cladding layer.

Author contribution All authors contributed to the study conception and design. Material preparation was performed by Lingling Xie and Zhengyi Jiang. Data collection and analysis were performed by Zhen Chang and Bing Long. Analysis was performed by Linhan Ouyang. The first draft of the manuscript was written by Shichao Zhu. Revision of the paper was performed by Feihong Yin. All authors commented on previous versions of the manuscript. All authors read and approved the final manuscript.

Funding This work was supported by the China Postdoctoral Science Foundation (Grant No. 2022M721395) and National Natural Science Foundation of China (Grant No. 72072089). Author Shichao Zhu and Linhan Ouyang have received research support.

Declarations

Competing interests The authors declare no competing interests.

References

1. DebRoy T, Mukherjee T, Milewski JO, Elmer JW, Ribic B, Blecher J, Zhang W (2019) Scientific, technological and economic issues in metal printing and their solutions. *Nat Mater* 18:1026–1032
2. Martin JH, Yahata BD, Hundley JM, Mayer JA, Schaedler TA, Pollock TM (2017) 3D printing of high-strength aluminium alloys. *Nature* 549:365–369
3. DebRoy T, Wei HL, Zuback J, Mukherjee T, Zhang W (2018) Additive manufacturing of metallic components – process, structure and properties. *Prog Mater Sci* 92:112–224
4. Cao S, Gu DD, Shi Q (2017) Relation of microstructure, microhardness and underlying thermodynamics in molten pools of laser melting deposition processed TiC/Inconel 625 composites. *J Alloys Compd* 692:758–769
5. Nassar AR, Gundermann MA, Reutzel EW, Guerrier P, Krane MH, Weldon MJ (2019) Formation processes for large ejecta and interactions with melt pool formation in powder bed fusion additive manufacturing. *Sci Rep* 9:5038
6. Sanaei N, Fatemi A (2021) Defects in additive manufactured metals and their effect on fatigue performance: a state-of-the-art review. *Prog Mater Sci* 117:100724
7. Shu FY, Liu S, Zhao HY, He WX, Xu BS (2018) Structure and high-temperature property of amorphous composite coating synthesized by laser cladding FeCrCoNiSiB high-entropy alloy powder. *J Alloys Compd* 731:662–666
8. Zhou SW, Xu TY, Hu C, Wu H, Liu HL, Ma XQ (2021) Effect of different topologies on microstructure and mechanical properties of multilayer coatings deposited by laser cladding with Inconel 625 wire. *Surf Coat Technol* 425(15):127299
9. Li S, Zeng XY, Hu QW (2007) Study on evaluation method of mechanical property of laser cladding layers. *Hot Working Technology* 36(11):50–52

10. Wu YL (2016) An investigation into the mechanical properties of Ti6Al4V lattice structures manufactured using selective laser melting. Chongqing University, Chongqing
11. Sun YH, Zhou JZ, Sheng J, Huang S, Xu SQ, Li J, Xu GF (2017) Tensile property and fracture analysis of 2024–T351 aluminum alloys by cryogenic laser peening. *Chin J Lasers* 44(8):1–8
12. Harrison NJ, Todd L, Mumtaz K (2017) Thermal expansion coefficients in Invar processed by selective laser melting. *J Mater Sci* 52:10517–10525
13. Qiu C, Adkins NJE, Attallah MM (2016) Selective laser melting of Invar 36: microstructure and properties. *Acta Mater* 103:382–395
14. Asgari H, Salarian M, Ma H, Olubamiji A, Vlasea M (2018) On thermal expansion behavior of Invar alloy fabricated by modulated laser powder bed fusion. *Materials&Design* 160:894–905
15. Ma MY, Xiong WJ, Lian Y, Han D, Zhao C, Zhang J (2020) Modeling and optimization for laser cladding via multi-objective quantum-behaved particle swarm optimization algorithm. *Surf Coat Technol* 381:125129
16. Lian GF, Yao MP, Zhang Y, Chen CR (2018) Analysis and prediction on geometric characteristics of multi-track overlapping laser cladding. *Int J Adv Manuf Technol* 97:2397–2407
17. Liu H, Du XT, Guo HF, Liu J, Chen PJ, Yang YF, Hao JB (2021) Finite element analysis of effects of dynamic preheating on thermal behavior of multi-track and multi-layer laser cladding. *Int J Light Electron Optics* 228:166194
18. DebRoy T, Mukherjee T, Wei HL, Elmer JW, Milewski JO (2021) Metallurgy, mechanistic models and machine learning in metal printing. *Nat Rev Mater* 6:48–68
19. Wang T, Zhu YY, Zhang SQ, Tang HB, Wang HM (2015) Grain morphology evolution behavior of titanium alloy components during laser melting deposition additive manufacturing. *J Alloys Compd* 632:505–513
20. Wang DS, Yang H, Yue LY, Zhang PP (2021) Effects of heat accumulation on temperature field during multi-track laser cladding of preset MCrAlY coating. *Mater Sci Forum* 1020:157–163
21. Gan ZT, Yu G, He XL, Li SX (2017) Numerical simulation of thermal behavior and multicomponent mass transfer in direct laser deposition of Co-base alloy on steel. *Int J Heat Mass Transf* 104:28–38
22. Alam MK, Urbanic RJ, Nazemi N, Edrissy A (2018) Predictive modeling and the effect of process parameters on the hardness and bead characteristics for laser-cladded stainless steel. *Int J Adv Manuf Technol* 94(1–4):397–413
23. Cheng YH, Cui R, Wang HZ, Han ZT (2017) Effect of processing parameters of laser on microstructure and properties of cladding 42CrMo steel. *Int J Adv Manuf Technol* 96(5–8):1–10

Publisher's Note Springer Nature remains neutral with regard to jurisdictional claims in published maps and institutional affiliations.

Springer Nature or its licensor (e.g. a society or other partner) holds exclusive rights to this article under a publishing agreement with the author(s) or other rightsholder(s); author self-archiving of the accepted manuscript version of this article is solely governed by the terms of such publishing agreement and applicable law.